1   **Novel nanostructured iron oxide cryogels for arsenic (As(III)) removal**

2

3   Lila Otero-González[a], Sergey V. Mikhalovsky[b,c], Miroslava Václavíková[d], Mikhail V.

4   Trenikhin[e], Andrew B. Cundy[a,1] and Irina N. Savina[f,*]

5

6   [a]School of Environment & Technology, University of Brighton, Brighton BN2 4GJ, UK

7   [b]ANAMAD Ltd, Sussex Innovation Centre Science Park Square, Falmer, Brighton BN1

8   9SB, UK

9   [c] Chuiko Institute of Surface Chemistry, 17, General Naumov street, Kyiv, 03164,

10   Ukraine

11   [d]Institute of Geotechnics, Slovak Academy of Sciences, 040 01 Košice, Slovakia

12   [e]Center of New Chemical Technologies of the Federal Research Center Boreskov

13   Institute of Catalysis of Siberian Branch of the Russian Academy of Sciences, Omsk

14   644040, Russia

15   [f]School of Pharmacy & Biomolecular Sciences, University of Brighton, Brighton BN2

16   4GJ, UK

17

18   [*]Corresponding author: Tel. +44 1273 642034; Fax. +44 1273 642674

19   E-mail: i.n.savina@brighton.ac.uk

20

21   Present address:

22   [1]Ocean and Earth Science, National Oceanography Centre Southampton, University of

23   Southampton, Southampton SO14 3ZH, UK

24   **ABSTRACT**

25   Novel macroporous iron oxide nanocomposite cryogels were synthesized and assessed as

26   arsenite (As(III)) adsorbents. The two-step synthesis method, by which a porous

27   nanonetwork of iron oxide is firstly formed, allowed a homogeneous dispersion of the

28   iron oxide in the cryogel reaction mixture, regardless of the nature of the co-polymer

29   forming the cryogel structure. The cryogels showed excellent mechanical properties,

30   especially the acrylamide-based cryogel. This gel showed the highest As(III) adsorption

31   capacity, with the maximum value estimated at 118 mg/g using the Langmuir model. The

32   immobilization of the nanostructured iron oxide gel into the cryogel matrix resulted in

33   slower adsorption kinetics, however the cryogels offer the advantage of a stable three-

34   dimensional structure that impedes the release of the iron oxide nanoparticles into the

35   treated effluent. A preliminary toxicity evaluation of the cryogels did not indicate any

36   apparent inhibition of human hepatic cells activity, which together with their mechanical

37   stability and high adsorption capacity for As(III) make them excellent materials for the

38   development of nanoparticle based adsorption devices for drinking water treatment.

39   **Keywords:** Iron oxide nanoparticles; Adsorbent; Arsenic; Water remediation; Polymer

40   cryogel

41

1. Introduction

Arsenic is a highly toxic metalloid ubiquitously present in the environment. Arsenic can cause severe health effects including skin problems, nerve damage and increased cancer risk, especially for lung, bladder, kidney and liver cancers [1]. Arsenic pollution in groundwater—originating from both anthropogenic and natural causes—is a concern in many regions of the world, including Bangladesh, India, Mexico and the United States (US), among others [2, 3]. The groundwater in these regions can contain arsenic concentrations as high as several mg/L [3], while both the guideline value proposed by the World Health Organization and the safe drinking water level set by the US Environmental Protection Agency is as low as 10 µg/L [4, 5]. As a result, the population in these regions are continuously exposed to levels of arsenic that can lead to chronic health conditions.

The removal of arsenic, and particularly arsenite (As(III)) from water, to concentrations below the maximum allowed level remains a challenge. There are a number of different approaches for arsenic remediation including adsorption, membrane filtration, coagulation-flocculation and ion exchange [6, 7]. Among these, adsorption has been reported as the most widely used technique for arsenic removal because of several advantages such as high arsenic removal efficiency, easy operation, and cost-effectiveness [3, 6, 8].

Advances in nanotechnology have allowed the development of a range of engineered nanomaterials (ENMs) for the remediation of contaminated water [9]. The increased specific surface area of ENMs significantly improves their adsorption capacity compared

3

65 with bulk materials [10-12]. Specifically, Fe-based nanoparticles (NPs) are an effective

66 adsorbent of a wide range of organic compounds, metals and metalloids including arsenic

67 [3, 8, 13-17]. However, the use of free, or unbound, NPs in water treatment creates an

68 extra technological challenge because of the need for subsequent NP separation from the

69 treated effluent. Moreover, potential risks of NPs to human health and the environment

70 raise concerns regarding their application in water treatment [18]. Nanocomposites may

71 overcome these limitations as they retain the advantages of free NPs while facilitating

72 their application (and recovery) in water treatment [19, 20].

73   Different nanocomposites have been developed based on the immobilization of Fe-

74 containing NPs on various matrices [21]. Among these, polymeric nanocomposites offer

75 advantageous properties such as large porosity, mechanical strength and diverse

76 geometries [22-25]. In particular, iron oxide (IO) NPs incorporated in polymeric beads

77 are commercially available for use in packed bed configurations [26-29]. Cryogelation is

78 a versatile technique that allows the preparation of mechanically robust polymer gels in

79 various shapes (e.g., monoliths, discs or beads). More importantly, cryogelation creates a

80 network of highly interconnected large macropores, up to 200 µm in diameter, in the

81 polymer gels, resulting in materials with high permeability and low flow-through

82 resistance.

83   Dispersing NPs homogeneously in the support matrix without a loss of reactivity

84 remains a challenge for polymeric and other nanocomposite systems [30]. Previously,

85 Fe_2O_3 and Fe_3O_4 NP were successfully dispersed as agglomerates, at relatively low IO

86 loadings of 0.059–0.095 g/g hydrated gel, in a poly(hydroxyethyl- methacrylate) cryogel,

87 in which the presence of poly(ethylene glycol) diacrylate possibly improved the NP

4

88 dispersion [31]. However, a direct synthesis route proved unsuitable for other types of

89 cryogels (e.g., acrylamide cryogels) [30]. Innovative synthetic methods are therefore

90 needed to improve the loading, dispersion and reactivity of NPs embedded into polymer

91 nanocomposites [30].

92   The objective of this study was the synthesis of an Fe-based nanocomposite using a

93 two-step method: synthesis of an IO-nanostructured gel followed by its dispersion in a

94 cryogel matrix. This method was developed to achieve a homogeneous dispersion of IO

95 gel particles in the material. The resulting cryogels were assessed for their potential

96 application in water treatment, particularly for the removal of an important groundwater

97 pollutant, As(III).

98

99 **2. Materials and Methods**

100

101 *2.1. Chemicals*

102

103   N,N'-methylenebisacrylamide (MBAA, 96%), 2-hydroxyethyl methacrylate (HEMA,

104 97%), N,N,N',N'-tetramethylethylenediamine (TEMED, 99%), iron(III) chloride

105 hexahydrate (FeCl$_3$·6H$_2$O, >99%), and As(III) trioxide (As$_4$O$_6$) were obtained from

106 Acros Organics (New Jersey, NJ, USA). Acrylamide (AAm, 97%), poly(ethylene glycol)

107 diacrylate (PEGDA, Mn ~ 250), and ammonium persulfate (APS, >98%) were sourced

108 from Sigma-Aldrich (St. Louis, MO, USA). Propylene oxide (>99%) was from Fisher

109 Chemical (Waltham, MA, USA).

110

2.2. Synthesis of iron oxide gel

FeCl$_3$·6H$_2$O (4.35 g) was dissolved in ethanol (50 mL). Polypropylene oxide (16.65 g) was added and the gel was left to age for 24 h at room temperature. Then, the gel was stirred with a spatula and strained through a 500-µm net. The IO gel particles were washed three times each with ethanol and deionized (DI) water by repeating cycles of mixing and centrifugation (4,400 rpm for 10 min). Finally, excess water was removed by centrifugation and the gel particles were used in subsequent experiments. The dry weight content of the IO gel varied from 2.5 to 8.5% for different batches.

2.3. Synthesis of macroporous monolithic cryogels

Monolithic macroporous hybrid cryogels were prepared by co-polymerization of the main monomer (AAm or HEMA) with a crosslinker (MBAA or PEGDA) under cryogenic conditions. Two types of cryogels were prepared: AAm with MBAA and HEMA with PEGDA. The monomers were dissolved in DI water with the monomer ratio given in Table 1. Different amounts of hydrated IO gel were mixed with the monomer solution and the mixture was degassed in an ultrasonic bath for 10 min. Then, TEMED and APS (1.2 wt.% of monomers) were added. Aliquots (1–2 mL) of the reaction solution were quickly added into separate glass tubes (80 × 11 mm ID) closed at the bottom with a silicone cap. The solution in the tubes was frozen in a thermostatic ethanol bath (Julabo F34-ED, Seelbach, Germany) at -12 °C for ca. 18 h and then thawed at room temperature.

133   The caps were removed and the cryogels were washed by passing an excess of DI water

134   through each sample.

135

136   *2.4. Transmission and scanning electron microscopy*

137

138   For transmission electron microscopy (TEM) imaging of IO gel, a freeze-dried

139   sample was ground to fine powder in an agate mortar and dispersed in ethanol. The

140   dispersion was sprayed over a copper TEM grid with a lacey carbon film. Electron

141   diffraction of the selected area (SAED) was carried out using a TEM instrument (JEM-

142   2100, JEOL Ltd, Tokyo, Japan) operating at 200 kV using a LaB_6 filament (the point-to-

143   point resolution of the microscope was 0.2 nm). The energy dispersive spectroscopy

144   (EDS) analysis was done with an X-ray spectrometer INCA (Oxford Instruments,

145   Abingdon, UK). The electron diffraction patterns and Fourier electron diffraction patterns

146   were obtained and processed using the Digital Micrograph software (Gatan Inc.,

147   Pleasanton, CA, USA). The calibration was carried out using the crystal lattice of gold

148   NPs. In addition, the X-ray powder diffraction (XRD) pattern of the IO gel sample was

149   carried out on a Bruker D8 Advance X-ray diffractometer with monochromatized Cu Kα

150   radiation, voltage and incandescent current of 40kV and 40mA, respectively, and scan

151   step of 0.02º (2θ) (Figure S1.

152

153   Alternatively, IO cryogels were dehydrated by washing with ethanol solutions of

154   increasing concentration (10, 20, 30, 50 and 75%) for 20 min each and dried in absolute

155   ethanol. Then, ethanol was replaced with propylene oxide, which was further replaced

7

156   with a low viscosity resin (TAAB Laboratories Equipment Ltd, Reading, UK). After

157   complete replacement, the resin was polymerized at 60 °C. Thin sections (100 nm) were

158   cut using an ultramicrotome (Leica Microsystems, Wetzlar, Germany), collected on

159   nickel support grids and examined by TEM (Hitachi-7100, Hitachi, Tokyo, Japan) at 100

160   kV. Images were acquired digitally with an axially mounted (2K $\times$ 2K pixel) camera

161   (Gatan Ultrascan 1000 CCD, Gatan Inc.).

162

163   Samples for scanning electron microscopy (SEM) were freeze-dried overnight.

164   Specimens were mounted on aluminum stubs fitted with adhesive carbon pads, sputter

165   coated with platinum and examined using a Zeiss NTS EVO or Zeiss NTS Sigma FEG

166   scanning electron microscope (Zeiss, Oberkochen, Germany).

167

168   *2.5. Specific surface area*

169

170   Samples were freeze-dried overnight and nitrogen adsorption-desorption isotherms

171   were measured using an Autosorb-1 gas sorption system (Quantachrome Instruments,

172   Boynton Beach, FL, USA) at 77.4 K. The data were analyzed using the Quantachrome

173   ASiQwin software. The specific surface area and pore volume were calculated using the

174   Brunauer-Emmett-Teller (BET) equation (Figure S2).

175

176   *2.6. Permeability measurements*

177

178   The flow rate of DI water passing through the column was measured at a constant

179   hydrostatic pressure equal to a 100-cm head of water-column, which corresponds to a

180   pressure of ca. 0.01 MPa on the cryogel composite [32].

181

182   *2.7. Mechanical properties*

183

184   The mechanical properties of the cryogels were tested using a TA.XTPlus Texture

185   Analyzer (Stable Micro Systems, Godalming, UK). The gels (9-mm diameter cylinders)

186   were placed between two compression plates and compressed with a steadily increasing

187   compression pressure of 5 N/min to the maximum loading of 18 N. All samples were

188   tested at room temperature. The compression modulus at 0.1 strain was calculated using

189   the TA.XTPlus software.

190

191   *2.8. As(III) solution preparation*

192

193   A stock solution of As(III) was prepared by dissolving As_4O_6 (2.5 g) in a sodium

194   hydroxide solution (2 g in 20 mL of DI water), which was then diluted with DI water to

195   200 mL. The pH was adjusted to 6.5 and 2 g of sodium bicarbonate were added. The final

196   volume was made up to 500 mL. The stock solution was used throughout all experiments

197   for preparation of As(III) solutions of varying dilutions.

198

199   *2.9. As(III) adsorption isotherms*

200

9

201   As(III) adsorption capacity of the IO gel and cryogels was evaluated in batch assays,

202   which were carried out in polypropylene tubes containing either 500 ± 20 mg of IO gel or

203   150 ± 20 mg of 2-mm square pieces of cryogels, and 40 or 20 mL of As(III) solution (pH

204     $= 7.5 \pm 0.3$), respectively. The tubes were shaken horizontally in an orbital shaker (150

205   rpm) at room temperature (24 ± 1 °C) for at least 48 h to ensure that equilibrium was

206   reached. Then, the tubes were centrifuged (4,400 rpm for 10 min) and liquid samples

207   were withdrawn and filtered through a 0.2-µm membrane before As analysis. Assays

208   were performed in duplicate. Control experiments with cryogels prepared without the

209   addition of IO were performed to evaluate the background As(III) adsorption on the

210   polymers.

211   The amount of As adsorbed was calculated from the difference between the initial

212   and equilibrium aqueous As concentration per 1 gram of adsorbent. The experimental

213   data were fitted to the Freundlich and Langmuir isotherm models.

214

215   *2.10. As(III) adsorption kinetics*

216

217   The kinetics of As(III) adsorption were evaluated in batch assays carried out in glass

218   flasks containing either 0.50 ± 0.01 g of IO gel or 1.40 ± 0.01 g of 2-mm square pieces of

219   IO/AAm/MBAA cryogel, and 200 mL of As(III) solution (ca. 9.5 mg/L, pH $= 7.5 \pm 0.3$).

220   The flasks were shaken in an orbital shaker (150 rpm) at room temperature (24 ± 1 °C).

221   Liquid samples were periodically withdrawn, filtered through a 0.2-µm membrane and

222   analyzed for As concentration. Assays were performed in duplicate. The experimental

223   data for As(III) adsorption kinetics on the IO/AAm/MBAA cryogel were analyzed using

224   several models of adsorption (i.e., pseudo-first order, pseudo-second order, intraparticle

225   diffusion, and liquid film diffusion) to obtain more information on the adsorption

226   mechanism [33].

227

228   *2.11. Toxicity analysis*

229

230   The toxicity of the gel and cryogels was assessed on human liver hepatocellular

231   carcinoma cells (HepG2). IO gel and cryogel leachates were prepared by incubation of

232   200 mg of gel or cryogel in 6 mL of minimum essential medium (MEM) supplemented

233   with 10% (v/v) fetal bovine serum (FBS) for 24 h at room temperature (24 ± 1 °C) and

234   shaking at 150 rpm. The leachates were filtered through a 0.2-µm membrane before

235   dosing to the cells.

236   HepG2 cells were routinely cultured in MEM with 10% (v/v) FBS at 37 °C in a 5%

237   CO_2 humidified atmosphere. Subsequently, the cells were transferred to 24-well plates at

238   a cell density of ca. 100,000 cells/cm^2 (ca. 200,000 cells per well) and incubated (37 °C,

239   5% CO_2) for 24 h. The spent medium was removed and the cells were dosed with 1 mL

240   of leachate. After 24 h of incubation, the cell viability and membrane damage were

241   assessed with the 3-(4,5-dimethylthiazol-2-yl)-2,5-diphenyltetrazolium bromide (MTT)

242   and lactate dehydrogenase (LDH) assays, respectively. The MTT assay was performed as

243   described elsewhere [34] and the LDH test as recommended by the kit manufacturer

244   (CytoTox 96® Non-Radioactive Cytotoxicity Assay, Promega, Madison, WI, USA).

245

246   *2.12. Analytical methods*

247

248   As and Fe were analyzed by inductively coupled plasma-optical emission

249   spectroscopy (ICP-OES Optima 2100 DV, Perkin Elmer, Waltham, MA, USA) at

250   wavelengths of 188.979 and 238.204 nm and with detection limits of 1–10 and <0.1

251   µg/L, respectively. The Fe content in the gel and cryogels was determined after acid

252   digestion with 6 M HCl.

253

254   **3. Results and Discussion**

255   *3.1. Nanostructured iron oxide gel*

256

257   Nanostructured IO hydrogels were prepared by a sol–gel process using a Fe(III) salt

258   as a precursor and propylene oxide as a gelation promoter. The propylene oxide acts as an

259   acid scavenger extracting protons from the hydrated Fe(III) species (Scheme 1). Contrary

260   to strong bases, propylene oxide increases the pH of the Fe(III) solution slowly and

261   uniformly. The slow reaction leads to the precipitation of uniform small IO particles

262   forming a porous monolithic IO gel structure [35, 36].
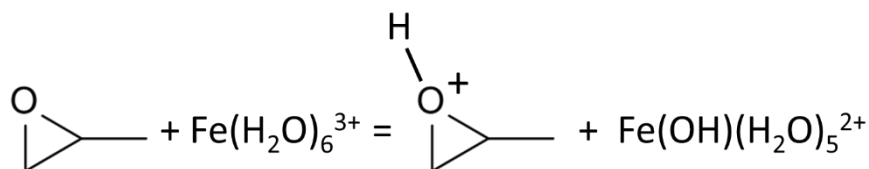
263   (1)

264

265   SEM images showed that the IO gel contained nanometer sized particles that formed

266   agglomerates with a size in the range of a few micrometers (Figure 1). TEM imaging

267   revealed that the IO gel particles measured approximately 5 nm (Figure 2A and B). The

268   particles had some degree of crystallinity, with the lattices in a d-spacing of ~2.53 Å

269   (Figure 2C), which fits well to that of the (311) lattice plane of maghemite (γ-Fe_2O_3). The

270   SAED analysis detected three well-resolved diffraction rings (Figure 2D) indexed as the

271   (220), (311) and (400) planes and corresponding to the distances of 2.95, 2.52 and 2.09

272   Å, respectively, in the crystal lattice of γ-Fe_2O_3. XRD analysis confirmed the presence of

273   maghemite (Figure S1). X-ray elemental mapping showed homogeneous distribution of

274   Fe and O in the IO gel (Figure 3).

275   The analysis of the IO gel surface showed a high specific surface area (S_{BET}) of 250

276   m^2/g and a total pore volume of 0.29 cm^3/g, of which 6.45×10^{-2} cm^3/g were nanopores

277   (Figure S2). The high S_{BET} value results from the sol–gel synthesis technique. The slow

278   polymerization leads to formation of a nanostructured gel, with a similar surface area to

279   that of free IO NPs [37].

280

281   *3.2. Macroporous monolithic composites with iron oxide gel*

282

283   The mechanical weakness of the IO gel hampers its direct application in water

284   treatment. The gel remains fragile after drying and lacks any defined permeable structure,

285   which makes it unsuitable for the design of water filtration devices. Thus, the IO gel was

286   embedded in a 3D scaffold using the cryogelation technique and forming a composite

287   monolithic polymer with high permeability and robust mechanical properties.

288   Cryogelation, defined as the formation of gels in a semi-frozen reaction solution, allows

289   the production of macroporous monolithic polymers with an interconnected porous

290   structure [38]. During cryogelation, the ice crystals formed at -12 °C expel the

291   polymerization reagents and the IO gel particles dispersed in the monomer mixture to the

292   remaining non-frozen liquid. The polymerization continues in these non-frozen regions,

293   where reagents are highly concentrated. After thawing, the voids left by the ice crystals

294   form an interconnected pore system, resulting in a highly porous polymer monolith.

295   Because of the relative slow freezing rate of the solution, large ice crystals form, leaving

296   pores with a size range of 1–100 µm [39]. The large interconnected pores provide high

297   permeability and allow effective flow-through of aqueous solutions through the cryogel

298   monolith, which could be used as a filter for water purification.

299   SEM imaging showed the macroporous structure of IO/HEMA/PEGDA and

300   IO/AAm/MBAA cryogel monoliths (Figure 4), with pore sizes of 20–100 µm and thin

301   polymer walls where the IO gel particles are embedded. The incorporation of IO in the

302   form of a nanostructured gel resulted in an even distribution of IO particles inside the

303   polymer walls, as shown in TEM images (Figure 5), and prevented agglomeration of the

304   IO NPs that was previously observed during IO cryogel composites preparation [31]. The

305   increase in the IO gel content resulted in a higher density of uniformly distributed IO

306   particles in the matrix (Figure 5C).

307   The IO composite cryogels had good mechanical properties, maintained their shape

308   and had low water flow resistance. The mechanical properties, assessed based on the

309   compression of the monoliths, depend on the monomer composition and the IO gel

310   content (Table 2). In general, the AAm/MBAA cryogels were less compressible, as their

311   Young's moduli were up to 10-times higher than those of the HEMA/PEGDA cryogels.

312   The addition of IO gel resulted in a decrease in the Young's modulus value of both types

313   of cryogels. The Young's moduli of IO/AAm/MBAA cryogels were between 41 and 82

314   kPa, while the blank counterpart ranged between 67 and 156 kPa. Significantly, the

315   IO/AAm/MBAA composites were stronger than the blank HEMA/PEGDA cryogels. This

316   indicates that AAm/MBAA cryogels will perform mechanically better under pressure in a

317   flow-through column system.

318   Macropores create a system of interconnected channels that provide low resistance to

319   the flow-through of liquid. The water flow through a column of IO/AAm/MBAA cryogel

320   was linear to the pump setting and no significant head loss was observed up to a flow rate

321   of 15 mL/min (Figure 6). Then, the flow rate decreased rapidly, although the column was

322   not visibly compressed. The decrease in the flow rate is probably the result of the

323   intrinsic compression and closure of the smallest channels in the cryogel.

324

325   *3.3. As(III) adsorption*

326   The total As(III) adsorption capacity of the IO gel and cryogels was assessed at

327   different monomer and IO gel concentrations (Table 3). The embedding of the IO gel

328   inside the cryogel matrix resulted in a 50% decrease of the original adsorption capacity of

329   the IO gel. The adsorption capacity of the IO/HEMA/PEGDA cryogels with maximal IO

330   load was 1.5-1.78 mg/g while for the IO gel it was 3.0 mg/g. The As(III) adsorption

331   increased with the concentration of IO gel in the cryogels. At a similar IO gel

332   concentration (ca. 70%), IO/HEMA/PEGDA and IO/AAm/MBAA showed a similar

333   As(III) adsorption capacity (1.30 ± 0.05 and 1.18 ± 0.10 mg/g of swollen cryogel,

334   respectively). Higher concentrations of IO gel could be reached in the HEMA/PEGDA

335   cryogel, but the poor mechanical properties of the IO/HEMA/PEGDA cryogels at these

336   high IO gel concentrations (Table 2) make them unsuitable for practical application.

15

337   Overall, the proposed method for the preparation of the IO cryogel composites produces

338   materials with much higher As(III) adsorption capacity compared to previously published

339   results [31]. The α-Fe$_2$O$_3$/HEMA/PEDGA and Fe$_3$O$_4$/HEMA/PEDGA cryogels prepared

340   by embedding α-Fe$_2$O$_3$ and Fe$_3$O$_4$ NPs (20 nm) inside a HEMA/PEDGA cryogel

341   containing 0.08% dry weight IO [31] showed a maximum As(III) adsorption capacity of

342   0.2 mg/g of swollen cryogel (Table 3). Thus, this new method allows the synthesis of

343   nanocomposite cryogels with significantly higher IO NP loading and improved

344   mechanical characteristics for As(III) adsorption.

345

346   *3.4. Maximum As(III) adsorption capacity*

347

348   Figure 7 shows the equilibrium isotherms of As(III) adsorption on the IO gel and

349   cryogels. The free IO gel displayed the highest As(III) adsorption capacity per dry weight

350   (Figure 7A). For example, the amount of As(III) adsorbed on the IO gel was between 2-

351   and 3-fold larger than that on the IO/AAm/MBAA cryogel and between 5- and 8-fold

352   larger than that on the IO/HEMA/PEGDA cryogel (Figure 7A). The IO gel had a larger

353   Fe content per dry weight (58–63%) compared with the IO/AAm/MBAA (19%) and

354   IO/HEMA/PEGDA (10%) cryogels, which explains the higher As(III) adsorption on the

355   free IO gel.

356   Based on the low As(III) adsorption observed in control cryogels without IO (Table

357   3), most of the As(III) adsorption is assumed to occur on IO sites, so the As(III) capacity

358   was normalized by the Fe content of each material to compare the IO performance. When

359   normalized per Fe mass, the As(III) adsorption capacity of the three materials was similar

360 (Figure 7B). For example, the amount of As(III) adsorbed on the IO gel was in the range

361 of 1.0- to 1.5-times the amount of As(III) adsorbed on the IO/AAm/MBAA cryogel. In

362 the case of the IO/HEMA/PEGDA cryogel, the As(III) adsorption was comparable to that

363 of the IO gel and IO/AAm/MBAA cryogel at equilibrium As(III) concentrations below

364 100 mg/L. However, due to the lower Fe content, the IO/HEMA/PEGDA cryogel reached

365 saturation at As(III) concentrations lower than the other two materials (Figure 7B). The

366 similar As(III) adsorption capacity per Fe mass is indicative of the near full availability of

367 the embedded IO as adsorption sites in the cryogels.

368   The adsorption isotherms have the shape of Type I adsorption isotherms. The

369 experimental data were fitted to the Langmuir and Freundlich adsorption models. In

370 general, the data fitted better to the Langmuir model indicating the formation of a

371 homogeneous monolayer (Table 4). Additionally, the estimated maximum adsorption

372 values (q_{max}) confirmed the similar As(III) capacity per Fe mass of the IO gel and

373 IO/AAm/MBAA cryogel. Specifically, the q_{max} values obtained were 625 and 588 mg

374 As(III) per g of Fe for the IO gel and the IO/AAm/MBAA cryogel, respectively (Table

375 4).

376   IO-based materials typically show remarkable As adsorption capacities, although the

377 reported values vary by several orders of magnitude among materials (Table 5). For

378 example, previous studies reported As(III) adsorption capacities of Fe_3O_4 NPs as low as

379 8.2 mg/g and as high as 175 mg/g [40, 41]. The variability depends most likely on iron

380 species, size, geometry, and carrier material, among other factors [8, 15]. Carbon

381 materials such as activated carbon and graphene oxide have been widely used as carriers

382 for IO nanomaterials, possibly because activated carbon is a material with high surface

383 area well established as a water treatment technology [42-44]. Other researchers opted for

384 natural materials such as sand and diatomite as IO carriers [45, 46]. Polymers such as

385 chitosan, alginate, poly(vinyl alcohol) and cellulose have also been used, with As

386 adsorption capacities ranging from 7.24 to 66.7 mg/g of material [47-50]. Typically, the

387 immobilization of the IO into the composite material decreases the As adsorption

388 capacity per IO mass, resulting in a tradeoff between high capacity and structural

389 properties [31, 49].

390

391 *3.5. Kinetics of As(III) adsorption*

392

393 The kinetics of As(III) adsorption were evaluated on the IO gel and IO/AAm/MBAA

394 cryogel, which was the cryogel with the highest adsorption capacity and best mechanical

395 properties. As(III) adsorption was very fast on the IO gel and about 90% As(III) removal

396 was achieved after only 15 min (Figure 8). On the other hand, adsorption kinetics were

397 slower on the IO/AAm/MBAA cryogel. For instance, 55% As(III) removal was attained

398 after 15 min. After 24 h, the As(III) removal was comparable between the two adsorbents

399 (ca. 96.5%, data not shown).

400 Slower adsorption kinetics are typically reported for cryogel-embedded particles [51-

401 54]. For example, the equilibrium of cadmium adsorption was reached four times more

402 slowly on titanate nanotubes embedded in a polyacrylamide cryogel compared with free

403 nanotubes [52]. Similarly, lead adsorption onto cryogel-embedded TiO_2 NPs was ca. 4-

404 fold slower than using free NPs before it reached equilibrium [54]. The slower adsorption

18

405 kinetics on cryogel nanocomposites are attributed to restricted accessibility of the

406 adsorption sites, which are dispersed in the polymeric matrix [31].

407   The analysis of the kinetic data of As(III) adsorption on the IO/AAm/MBAA cryogel

408 shows that the pseudo-second order model fits the experimental data better than any other

409 model (Table 6). Previously, it was shown before that the pseudo-second order equation

410 for adsorption kinetics is more similar to the rate law for a chemical reaction, thus the

411 fitting of our experimental data to this model could indicate that the adsorption occurs

412 mainly via a simple chemical reaction between As(III) and functional groups on the IO

413 surface. The data were also analyzed using intraparticle diffusion and liquid film

414 diffusion models to establish the rate determining step for As(III) adsorption (Table 6).

415 The intercept values were 6.34 mg/g with $R^2 = 0.913$ and 0.901 mg/g with $R^2 = 0.953$ for

416 intraparticle diffusion and liquid film diffusion models, respectively, suggesting that the

417 adsorption process might follow intraparticle diffusion as well as film diffusion, with the

418 latter playing a more significant role.

419   The adsorption of As(III) by IO gel was confirmed by an FT-IR study of the IO gel

420 before and after adsorption of As(III) (Figure S3). The wave number assigned to the

421 hydroxyl group at 3348 cm^{-1} for the IO gel shifted to 3226 cm^{-1} after the adsorption of

422 As(III) by the IO gel, as result of interaction with As(III). A new band appeared around

423 775 cm^{-1}, contributed by the As-O vibration. Other studies have shown that the

424 adsorption of As(III) by IO proceeds through formation of inner-sphere complexes

425 between arsenite and iron oxides [33].

426

427 *3.6. Toxicity analysis*

428

Nanocomposites intended for water treatment should be safe for human health and the environment. Particularly, the release of toxic components during application is a potentially serious issue both in terms of leaching of toxic gel components (e.g., acrylamide) and of nanoparticles [55]. Thus, the environmental and health risks of the materials were assessed by generating a leachate and evaluating its toxicity to human hepatic cells (HepG2), one of the most widely used human cell models for toxicity studies. In general, none of the leachates exhibited cell toxicity (Figure 9). The viability of HepG2 cells treated with the leachates was similar or even higher than that of the untreated control (Figure 9A). Moreover, none of the treatments suggests a negative effect of the leachates on the cell membrane (Figure 9B). Although an exhaustive risk assessment would be needed to ensure the safety of the cryogels, these preliminary results suggest a low risk of releasing toxic substances from the materials.

441

4. Conclusions

A novel two-step method enabled the synthesis of highly permeable macroporous nanocomposite cryogels with improved mechanical properties and adsorption capacity for As(III). The IO gel prepared by a sol-gel process has a well-developed nanostructure that was preserved during its embedding inside the 3D porous matrix of AAm/MBAA and HEMA/PEGDA cryogels, resulting in an even distribution of IO NPs in the cryogel matrix. The IO gel preserved its adsorption capacity after embedding inside the polymer. The analysis of adsorption data could be best described by a pseudo-second order kinetic model and the Langmuir adsorption isotherm. The maximum As(III) adsorption capacity

451   (q_{max}) of the IO/AAm/MBAA and IO/HEMA/PEGDA cryogels was 588 and 345 mg/g Fe

452   or 118 and 35.7 mg/g of dried composite, respectively, which is considerably higher than

453   that of α-Fe_2O_3/HEMA/PEDGA and Fe_3O_4/HEMA/PEDGA cryogels reported before.

454   The adsorption kinetics of the IO/AAm/MBAA cryogel were slower than those of the IO

455   gel. Although fast adsorption kinetics are advantageous, the use of free IO gel in water

456   treatment is impractical because of the complications that would arise from the separation

457   of the gel from the treated effluent. Their mechanical stability, low toxicity and low flow-

458   through resistance make the cryogels excellent candidates for the development of

459   nanocomposite adsorption devices for drinking water treatment.

460

461   **Acknowledgments**

462

467

468 **REFERENCES**

469 [1] M.F. Hughes, B.D. Beck, Y. Chen, A.S. Lewis, D.J. Thomas, Arsenic exposure and

470 toxicology: A historical perspective, Toxicol. Sci., 123 (2011) 305-332.

471 [2] A. Sarkar, B. Paul, The global menace of arsenic and its conventional remediation - A

472 critical review, Chemosphere, 158 (2016) 37-49.

473 [3] S.I. Siddiqui, M. Naushad, S.A. Chaudhry, Promising prospects of nanomaterials for

474 arsenic water remediation: A comprehensive review, Process Saf. Environ. Prot., 126

475 (2019) 60-97.

476 [4] Environmental Protection Agency, Drinking water standard for arsenic, 2001.

477 [5] World Health Organization, Guidelines for drinking-water quality: fourth edition

478 incorporating the first addendum, Geneva, 2017.

479 [6] N. Nicomel, K. Leus, K. Folens, P. Van Der Voort, G. Du Laing, Technologies for

480 arsenic removal from water: Current status and future perspectives, Int. J. Env. Res.

481 Public Health, 13 (2016) 62.

482 [7] D. Mohanty, Conventional as well as emerging arsenic removal technologies—a

483 critical review, Water, Air, Soil Pollut., 228 (2017) 381.

484 [8] S.I. Siddiqui, S.A. Chaudhry, Iron oxide and its modified forms as an adsorbent for

485 arsenic removal: A comprehensive recent advancement, Process Saf. Environ. Prot., 111

486 (2017) 592-626.

487 [9] P.J.J. Alvarez, C.K. Chan, M. Elimelech, N.J. Halas, D. Villagrán, Emerging

488 opportunities for nanotechnology to enhance water security, Nat. Nanotechnol., 13 (2018)

489 634−641.

22

490   [10] M. Hua, S. Zhang, B. Pan, W. Zhang, L. Lv, Q. Zhang, Heavy metal removal from

491   water/wastewater by nanosized metal oxides: A review, J. Hazard. Mater., 211–212

492   (2012) 317-331.

493   [11] M. Nagpal, R. Kakkar, Use of metal oxides for the adsorptive removal of toxic

494   organic pollutants, Sep. Purif. Technol., 211 (2019) 522–539.

495   [12] Y. Wu, H. Pang, Y. Liu, X. Wang, S. Yu, D. Fu, J. Chen, X. Wang, Environmental

496   remediation of heavy metal ions by novel-nanomaterials: A review, Environ. Pollut., 246

497   (2019) 608-620.

498   [13] P. Saharan, G.R. Chaudhary, S.K. Mehta, A. Umar, Removal of water contaminants

499   by iron oxide nanomaterials, J. Nanosci. Nanotechnol., 14 (2014) 627–643.

500   [14] K.K. Kefeni, B.B. Mamba, T.A.M. Msagati, Application of spinel ferrite

501   nanoparticles in water and wastewater treatment: A review, Sep. Purif. Technol., 188

502   (2017) 399-422.

503   [15] L. Hao, M. Liu, N. Wang, G. Li, A critical review on arsenic removal from water

504   using iron-based adsorbents, RSC Adv., 8 (2018) 39545–39560.

505   [16] Y. Chen, W. Liang, Y. Li, Y. Wu, Y. Chen, W. Xiao, L. Zhao, J. Zhang, H. Li,

506   Modification, application and reaction mechanisms of nano-sized iron sulfide particles

507   for pollutant removal from soil and water: A review, Chem. Eng. J., 362 (2019) 144-159.

508   [17] G.N. Hlongwane, P.T. Sekoai, M. Meyyappan, K. Moothi, Simultaneous removal of

509   pollutants from water using nanoparticles: A shift from single pollutant control to

510   multiple pollutant control, Sci. Total Environ., 656 (2019) 808-833.

511   [18] M.S. Mauter, I. Zucker, F. Perreault, J.R. Werber, J.-H. Kim, M. Elimelech, The role

512   of nanotechnology in tackling global water challenges, Nat. Sustain., 1 (2018) 166-175.

513 [19] B. Pan, B. Pan, W. Zhang, L. Lv, Q. Zhang, S. Zheng, Development of polymeric

514 and polymer-based hybrid adsorbents for pollutants removal from waters, Chem. Eng. J.,

515 151 (2009) 19-29.

516 [20] G. Lofrano, M. Carotenuto, G. Libralato, R.F. Domingos, A. Markus, L. Dini, R.K.

517 Gautam, D. Baldantoni, M. Rossi, S.K. Sharma, M.C. Chattopadhyaya, M. Giugni, S.

518 Meric, Polymer functionalized nanocomposites for metals removal from water and

519 wastewater: An overview, Water Res., 92 (2016) 22–37.

520 [21] W. Wong, H.Y. Wong, A.B.M. Badruzzaman, H.H. Goh, M. Zaman, Recent

521 advances in exploitation of nanomaterial for arsenic removal from water: A review,

522 Nanotechnology, 28 (2017) 042001.

523 [22] M.J. DeMarco, A.K. SenGupta, J.E. Greenleaf, Arsenic removal using a

524 polymeric/inorganic hybrid sorbent, Water Res., 37 (2003) 164–176.

525 [23] M. Hua, B. Yang, C. Shan, W. Zhang, S. He, L. Lv, B. Pan, Simultaneous removal

526 of As(V) and Cr(VI) from water by macroporous anion exchanger supported nanoscale

527 hydrous ferric oxide composite, Chemosphere, 171 (2017) 126-133.

528 [24] X. You, C. Valderrama, V. Soldatov, J.L. Cortina, Phosphate recovery from treated

529 municipal wastewater using hybrid anion exchangers containing hydrated ferric oxide

530 nanoparticles, J. Chem. Technol. Biotechnol., 93 (2018) 358–364.

531 [25] S. Tandorn, O.-a. Arqueropanyo, W. Naksata, P. Sooksamiti, I. Chaisri, Adsorption

532 of arsenate from aqueous solution by ferric oxide-impregnated Dowex Marathon MSA

533 anion exchange resin: application of non-linear isotherm modeling and thermodynamic

534 studies, Environ. Earth Sci., 78 (2019) 136.

535   [26] P. Sylvester, P. Westerhoff, T. Möller, M. Badruzzaman, O. Boyd, A hybrid sorbent

536   utilizing nanoparticles of hydrous iron oxide for arsenic removal from drinking water,

537   Environ. Eng. Sci., 24 (2006) 104−112.

538   [27] T. Möller, P. Sylvester, Effect of silica and pH on arsenic uptake by resin/iron oxide

539   hybrid media, Water Res., 42 (2008) 1760-1766.

540   [28] M.R. Boldaji, R. Nabizadeh, M.H. Dehghani, K. Nadafi, A.H. Mahvi, Evaluating the

541   performance of iron nanoparticle resin in removing arsenate from water, J. Environ. Sci.

542   Health A, 45 (2010) 946-950.

543   [29] Y. Jiang, M. Hua, B. Wu, H. Ma, B. Pan, Q. Zhang, Enhanced removal of arsenic

544   from a highly laden industrial effluent using a combined coprecipitation/nano-adsorption

545   process, Environ. Sci. Pollut. Res., 21 (2014) 6729−6735.

546   [30] I.N. Savina, G.C. Ingavle, A.B. Cundy, S.V. Mikhalovsky, A simple method for the

547   production of large volume 3D macroporous hydrogels for advanced biotechnological,

548   medical and environmental applications, Sci. Rep., 6 (2016) 21154.

549   [31] I.N. Savina, C.J. English, R.L.D. Whitby, Y. Zheng, A. Leistner, S.V. Mikhalovsky,

550   A.B. Cundy, High efficiency removal of dissolved As(III) using iron nanoparticle-

551   embedded macroporous polymer composites, J. Hazard. Mater., 192 (2011) 1002-1008.

552   [32] F.M. Plieva, I.N. Savina, S. Deraz, J. Andersson, I.Y. Galaev, B. Mattiasson,

553   Characterization of supermacroporous monolithic polyacrylamide based matrices

554   designed for chromatography of bioparticles, J. Chromatogr. B, 807 (2004) 129-137.

555   [33] S.I. Siddiqui, S.A. Chaudhry, Nanohybrid composite Fe_2O_3-ZrO_2/BC for inhibiting

556   the growth of bacteria and adsorptive removal of arsenic and dyes from water, J. Clean.

557   Prod., 223 (2019) 849-868.

558 [34] L. Otero-González, R. Sierra-Álvarez, S. Boitano, J.A. Field, Application and

559 validation of an impedance-based real time cell analyzer to measure the toxicity of

560 nanoparticles impacting human bronchial epithelial cells, Environ. Sci. Technol., 46

561 (2012) 10271-10278.

562 [35] A.E. Gash, T.M. Tillotson, J.H. Satcher, J.F. Poco, L.W. Hrubesh, R.L. Simpson,

563 Use of epoxides in the sol−gel synthesis of porous iron(III) oxide monoliths from Fe(III)

564 salts, Chem. Mater., 13 (2001) 999-1007.

565 [36] J.D. Walker, R. Tannenbaum, Characterization of the sol−gel formation of iron(III)

566 oxide/hydroxide nanonetworks from weak base molecules, Chem. Mater., 18 (2006)

567 4793-4801.

568 [37] M. Auffan, J. Rose, O. Proux, D. Borschneck, A. Masion, P. Chaurand, J.-L.

569 Hazemann, C. Chaneac, J.-P. Jolivet, M.R. Wiesner, A. Van Geen, J.-Y. Bottero,

570 Enhanced adsorption of arsenic onto maghemites nanoparticles: As(III) as a probe of the

571 surface structure and heterogeneity, Langmuir, 24 (2008) 3215-3222.

572 [38] V.M. Gun'ko, I.N. Savina, S.V. Mikhalovsky, Cryogels: Morphological, structural

573 and adsorption characterisation, Adv. Colloid Interface Sci., 187–188 (2013) 1-46.

574 [39] I.N. Savina, V.M. Gun'ko, V.V. Turov, M. Dainiak, G.J. Phillips, I.Y. Galaev, S.V.

575 Mikhalovsky, Porous structure and water state in cross-linked polymer and protein cryo-

576 hydrogels, Soft Matter, 7 (2011) 4276-4283.

577 [40] S. Luther, N. Borgfeld, J. Kim, J.G. Parsons, Removal of arsenic from aqueous

578 solution: A study of the effects of pH and interfering ions using iron oxide nanomaterials,

579 Microchem. J., 101 (2012) 30-36.

580 [41] C.T. Yavuz, J.T. Mayo, W.W. Yu, A. Prakash, J.C. Falkner, S. Yean, L. Cong, H.J.

581 Shipley, A. Kan, M. Tomson, D. Natelson, V.L. Colvin, Low-field magnetic separation

582 of monodisperse Fe_3O_4 nanocrystals, Science, 314 (2006) 964-967.

583 [42] H. Su, Z. Ye, N. Hmidi, R. Subramanian, Carbon nanosphere–iron oxide

584 nanocomposites as high-capacity adsorbents for arsenic removal, RSC Adv., 7 (2017)

585 36138-36148.

586 [43] H. Su, Z. Ye, N. Hmidi, High-performance iron oxide–graphene oxide

587 nanocomposite adsorbents for arsenic removal, Colloids Surf. Physicochem. Eng.

588 Aspects, 522 (2017) 161-172.

589 [44] Z. Wu, W. Li, P.A. Webley, D. Zhao, General and controllable synthesis of novel

590 mesoporous magnetic iron oxide@carbon encapsulates for efficient arsenic removal,

591 Adv. Mater., 24 (2012) 485-491.

592 [45] D. Afzali, M. Rouhani, F. Fathirad, T. Shamspur, A. Mostafavi, Nano-iron oxide

593 coated on sand as a new sorbent for removal of arsenic from drinking water, Desalin.

594 Water Treat., 57 (2016) 13030-13037.

595 [46] Y. Du, H. Fan, L. Wang, J. Wang, J. Wu, H. Dai, α-Fe_2O_3 nanowires deposited

596 diatomite: highly efficient absorbents for the removal of arsenic, J. Mater. Chem. A, 1

597 (2013) 7729-7737.

598 [47] S. Hasan, A. Ghosh, K. Race, R. Schreiber, M. Prelas, Dispersion of FeOOH on

599 chitosan matrix for simultaneous removal of As(III) and As(V) from drinking water, Sep.

600 Sci. Technol., 49 (2014) 2863-2877.

601 [48] N. Mahanta, S. Valiyaveettil, Functionalized poly(vinyl alcohol) based nanofibers

602 for the removal of arsenic from water, RSC Adv., 3 (2013) 2776-2783.

603 [49] A. Sigdel, J. Park, H. Kwak, P.-K. Park, Arsenic removal from aqueous solutions by

604 adsorption onto hydrous iron oxide-impregnated alginate beads, J. Ind. Eng. Chem., 35

605 (2016) 277-286.

606 [50] X. Yu, S. Tong, M. Ge, J. Zuo, C. Cao, W. Song, One-step synthesis of magnetic

607 composites of cellulose@iron oxide nanoparticles for arsenic removal, J. Mater. Chem.

608 A, 1 (2013) 959-965.

609 [51] L. Önnby, V. Pakade, B. Mattiasson, H. Kirsebom, Polymer composite adsorbents

610 using particles of molecularly imprinted polymers or aluminium oxide nanoparticles for

611 treatment of arsenic contaminated waters, Water Res., 46 (2012) 4111-4120.

612 [52] L. Önnby, K. Harald, I.A. Nges, Cryogel-supported titanate nanotubes for waste

613 treatment: Impact on methane production and bio-fertilizer quality, J. Biotechnol., 207

614 (2015) 58-66.

615 [53] R. Busquets, A.E. Ivanov, L. Mbundi, S. Hörberg, O.P. Kozynchenko, P.J. Cragg,

616 I.N. Savina, R.L.D. Whitby, S.V. Mikhalovsky, S.R. Tennison, H. Jungvid, A.B. Cundy,

617 Carbon-cryogel hierarchical composites as effective and scalable filters for removal of

618 trace organic pollutants from water, J. Environ. Manage., 182 (2016) 141-148.

619 [54] Y. Shu, R. Huang, X. Wei, L. Liu, Z. Jia, Pb(II) removal using TiO_2-embedded

620 monolith composite cryogel as an alternative wastewater treatment method, Water, Air,

621 Soil Pollut., 228 (2017) 375.

622 [55] L. Önnby, C. Svensson, L. Mbundi, R. Busquets, A. Cundy, H. Kirsebom, γ-Al_2O_3-

623 based nanocomposite adsorbents for arsenic(V) removal: Assessing performance, toxicity

624 and particle leakage, Sci. Total Environ., 473–474 (2014) 207-214.

625 [56] V. Fierro, G. Muñiz, G. Gonzalez-Sánchez, M.L. Ballinas, A. Celzard, Arsenic

626 removal by iron-doped activated carbons prepared by ferric chloride forced hydrolysis, J.

627 Hazard. Mater., 168 (2009) 430-437.

628 [57] A. Gupta, V.S. Chauhan, N. Sankararamakrishnan, Preparation and evaluation of

629 iron–chitosan composites for removal of As(III) and As(V) from arsenic contaminated

630 real life groundwater, Water Res., 43 (2009) 3862-3870.

631 [58] V. Lenoble, O. Bouras, V. Deluchat, B. Serpaud, J.-C. Bollinger, Arsenic adsorption

632 onto pillared clays and iron oxides, J. Colloid Interface Sci., 255 (2002) 52-58.

633 [59] S. Lin, D. Lu, Z. Liu, Removal of arsenic contaminants with magnetic γ-Fe_2O_3

634 nanoparticles, Chem. Eng. J., 211–212 (2012) 46-52.

635 [60] W. Tang, Q. Li, S. Gao, J.K. Shang, Arsenic (III,V) removal from aqueous solution

636 by ultrafine α-Fe_2O_3 nanoparticles synthesized from solvent thermal method, J. Hazard.

637 Mater., 192 (2011) 131-138.

638 [61] N. Gerard, R. Santhana Krishnan, S.K. Ponnusamy, H. Cabana, V.K. Vaidyanathan,

639 Adsorptive potential of dispersible chitosan coated iron-oxide nanocomposites toward the

640 elimination of arsenic from aqueous solution, Process Saf. Environ. Prot., 104 (2016)

641 185-195.

642

643   **Table 1.** Monomer molar ratio and total monomer content in the reaction mixture used

644   for the synthesis of the polymer cryogels.

Cryogel	Monomer molar ratio	Total monomer content in solution (wt.%)		
AAm:MBAA	8:1	6	8	12
HEMA:PEGDA	6:1	-	8	12

645

646   **Table 2.** Mechanical properties of the iron oxide composite cryogels.

	Monomer (wt.%)	Iron oxide gel (swollen wt.%)	Iron oxide gel (dry wt.%)	Young's modulus (kPa)
HEMA/PEGDA	8	0	0	16 ± 7
HEMA/PEGDA	12	67	1.68	11 ± 5
AAm/MBAA	6	0	0	66 ± 20
AAm/MBAA	6	50	1.25	56 ± 6
AAm/MBAA	6	70	1.75	40 ± 6
AAm/MBAA	8	0	0	155 ± 16
AAm/MBAA	8	50	1.25	81 ± 2
α-Fe_2O_3-HEMA/PEDGA[†]	8	NA[‡]	0.08	4.6 ± 1.3
Fe_3O_4-HEMA/PEDGA[†]	8	NA[‡]	0.08	6.0 ± 1.0

647   [†] Data from [31]

648   [‡] Contain iron NPs α-Fe_2O_3 (20 nm) or Fe_3O_4 (30 nm)

649

650 **Table 3.** Equilibrium As(III) adsorption by the iron oxide gel and cryogels. Data for

651 control cryogels without iron oxide are included for comparison. Initial As(III)

652 concentration was 10 mg/L.

	Monomer (wt.%)	Iron oxide gel (swollen wt.%)	Iron oxide gel (dry wt.%)	As(III) adsorption (mg/g swollen cryogel)
IO gel	NA	100	2.50	3.0 ± 0.2
control HEMA/PEGDA	8	NA	NA	0.04 ± 0.03
IO/HEMA/PEGDA	8	33	0.83	0.87 ± 0.05
IO/HEMA/PEGDA	12	67	1.68	1.30 ± 0.05
IO/HEMA/PEGDA	8	100	2.50	1.50 ± 0.10
IO/HEMA/PEGDA	12	100	2.50	1.78 ± 0.03
control AAm/MBAA	8	NA	NA	0.17 ± 0.12
IO/AAm/MBAA	6	50	1.25	0.92 ± 0.03
IO/AAm/MBAA	8	50	1.25	0.96 ± 0.05
IO/AAm/MBAA	6	70	1.75	1.18 ± 0.10
α-Fe$_2$O$_3$-HEMA/PEDGA[†]	8	NA[‡]	0.08	0.21 ± 0.03
Fe$_3$O$_4$-HEMA/PEDGA[†]	8	NA[‡]	0.08	0.23 ± 0.02

653 [†] Data from [31]

654 [‡] Contain iron NPs α-Fe$_2$O$_3$ (size = 20 nm) or Fe$_3$O$_4$ (size = 30 nm)

655

656 **Table 4.** Fitting parameters of Freundlich and Langmuir isotherm models for As(III)

657 adsorption onto iron oxide gel and composite cryogels (IO/AAm/MBAA: 8% monomer

658 and 50% IO gel; IO/HEMA/PEGDA: 8% monomer and 25% IO gel). The data are fitted

659 based on As(III) adsorption per dry weight and Fe weight. R^2 indicates goodness of fit.

	Freundlich model			Langmuir model		
	n	K_F $(mg/g)(L/mg)^{1/n}$	R^2	K (L/mg)	q_{max} (mg/g)	R^2
IO gel						
Dry weight	3.22	54.6	0.968	0.048	357	0.978
Fe weight	3.43	113	0.952	0.057	625	0.989
IO/AAm/MBAA						
Dry weight	3.44	21.9	0.943	0.035	118	0.950
Fe weight	3.38	99.5	0.943	0.027	588	0.960
IO/HEMA/PEGDA						
Dry weight	3.92	10.5	0.851	0.118	35.7	0.966
Fe weight	4.76	131	0.777	0.195	345	0.991

660

661   **Table 5.** Comparative maximum As(III) adsorption capacity of hybrid nanocomposites.

Adsorbent	Maximum capacity for As(III) adsorption (mg/g)	Reference
Fe-doped activated carbon	0.028	[56]
Sand coated with magnetic IO NPs	0.285	[45]
Hydrous IO-impregnated alginate beads	6.21	[49]
Chitosan beads with FeOOH NPs	7.24	[47]
Fe–chitosan composites	16.2	[57]
Fe_2O_3 NP cellulose composites	23.2	[50]
Hydrated ferric hydroxide	28	[58]
α-Fe_2O_3 nanowires deposited diatomite	60.2	[46]
Fe-functionalized poly(vinyl alcohol) based nanofibers	66.7	[48]
Magnetic γ-Fe_2O_3 NPs	74.8	[59]
Ultrafine α-Fe_2O_3 NPs	95	[60]
IO/AAm/MBAA cryogel	118	This study
IO–graphene oxide nanocomposites	147	[43]
Chitosan coated with IO nanocomposites	267	[61]

662

663 **Table 6.** Fitting parameters of different kinetic models for As(III) adsorption onto an iron

664 oxide composite cryogel (IO/AAm/MBAA: 8% monomer and 50% IO gel). The initial

665 As(III) concentration was ca. 10 mg/L. Values are presented as mg/g of dry weight. R^2

666 indicates goodness of fit.

Pseudo-first order		Pseudo-second order		Intraparticle diffusion		Liquid film diffusion	
k_1 (1/min)	0.012	k_2 (g/min·mg)	0.007	k_{ipd} (mg/g·min$^{0.5}$)	0.454	k_{fd} (mg/g·min)	0.010
q_e (mg/g)	7.55	q_e (mg/g)	12.7	C (mg/g)	6.34	C (mg/g)	0.901
R^2	0.880	R^2	0.999	R^2	0.913	R^2	0.953

667

FIGURE CAPTIONS

669 **Figure 1.** SEM images of the iron oxide gel at different magnifications: 5k $\times$

670 magnification (A) and 250k $\times$ magnification (B).

671 **Figure 2.** TEM images of an iron oxide gel particle (A) and higher magnification of the

672 area enclosed in the square (B). TEM image of the crystal lattice of an individual γ-Fe$_2$O$_3$

673 particle pointed by an arrow (C). Selected area electron diffraction (D) and X-ray

674 spectrum of the individual γ-Fe$_2$O$_3$ particle (E).

675 **Figure 3.** TEM image of the iron oxide gel (A) and distribution of elemental iron (B) and

676 oxygen (C).

677 **Figure 4.** SEM images of the IO/HEMA/PEGDA cryogel with a 100% IO gel content

678 (A) and IO/AAm/MBAA cryogel with a 33% IO gel content (B).

679 **Figure 5.** TEM image of a cross section of the IO/HEMA/PEGDA cryogel with a 33%

680 IO gel content (A and B) and with a 100% IO gel content (C).

681 **Figure 6.** Water flow rate through a 2-mL column of IO/AAm/MBAA cryogel compared

682 with the flow rate set in the pump.

683 **Figure 7.** Isotherms of As(III) adsorption on the IO gel (■), IO/AAm/MBAA cryogel (○)

684 and IO/HEMA/PEGDA cryogel (◊) expressed per dry weight (A) and Fe weight (B).

685 Solid/liquid contact was performed at neutral pH (7.5 ± 0.3) and room temperature (24 ±

686 1 °C). Dotted lines represent the Langmuir fitting of experimental data.

687 **Figure 8.** Kinetics of As(III) adsorption on the IO gel (■) and IO/AAm/MBAA cryogel

688 (○) at neutral pH (7.5 ± 0.1) and room temperature (24 ± 1 °C). The initial As(III)

689 concentration was ca. 9.5 mg/L.

690 **Figure 9.** Cell viability (A) and cell lysis (B) of HepG2 cells exposed for 24 h to

691 leachates of the IO gel and cryogels. Cell viability is expressed as percentage of non-

692 exposed (-) control. Cell lysis is expressed as percentage of completely lysed cells (1%

693 (v/v) Tryton X-100, (+) control).
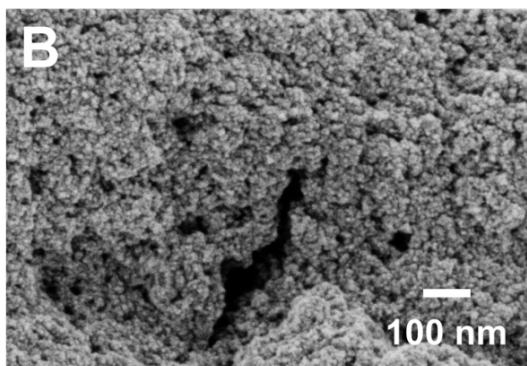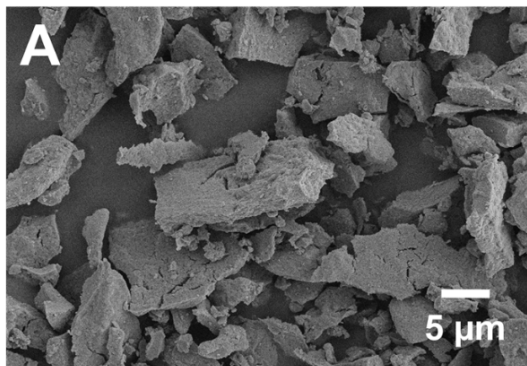
694

695

696

697

698

699

700

701

702

703

704

705

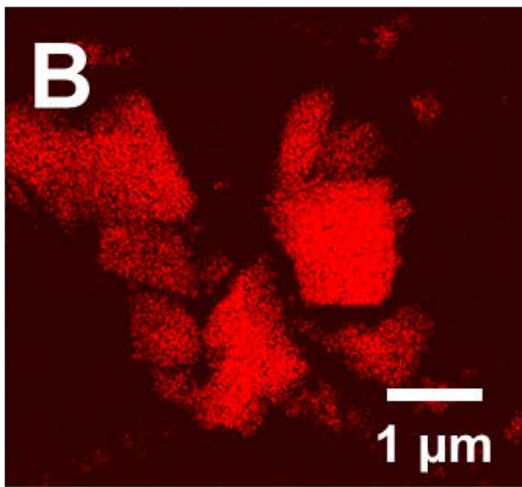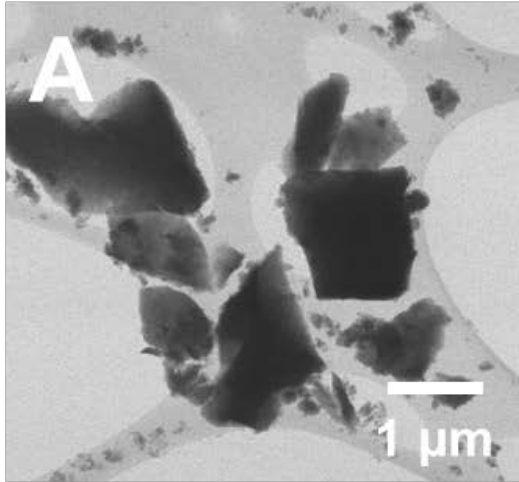706 **Figure 1**

707
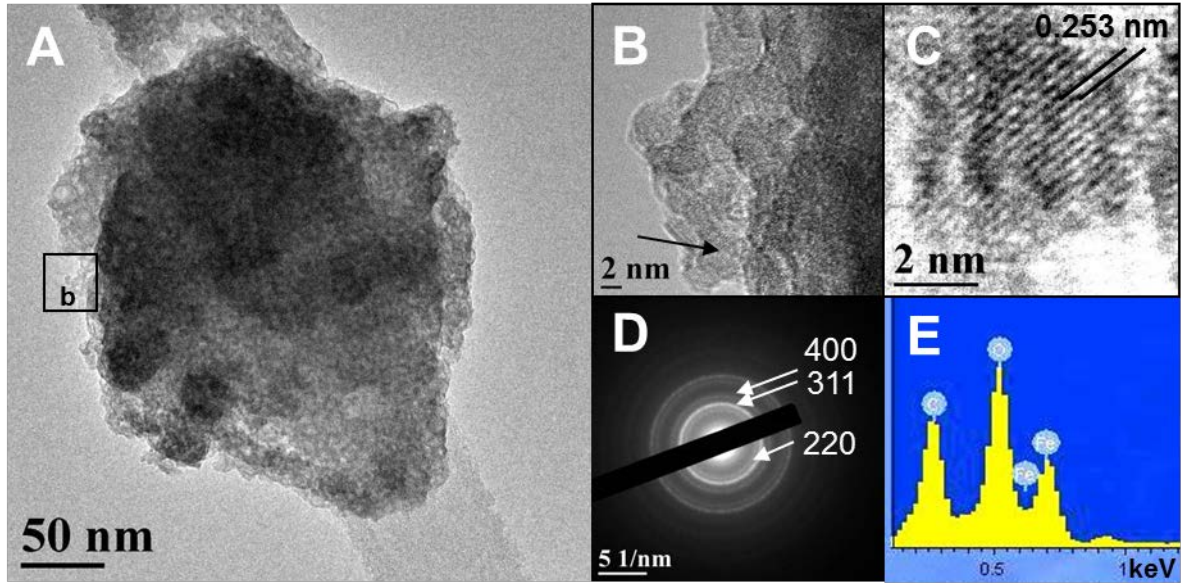
708

709

710

711

712

713

714

715

716

717

718

719 **Figure 2**

720
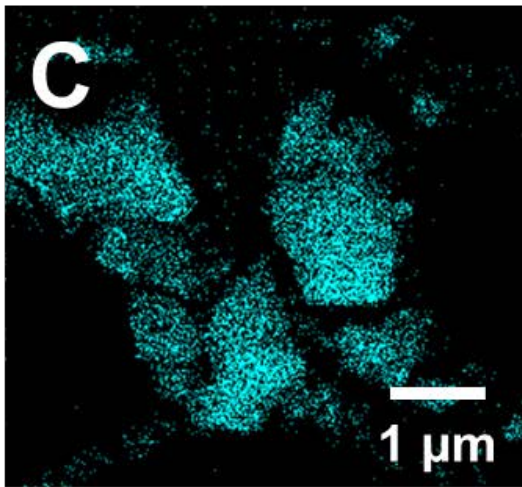
721

722

723   **Figure 3**

724
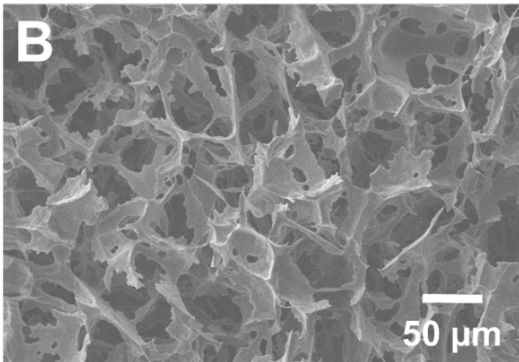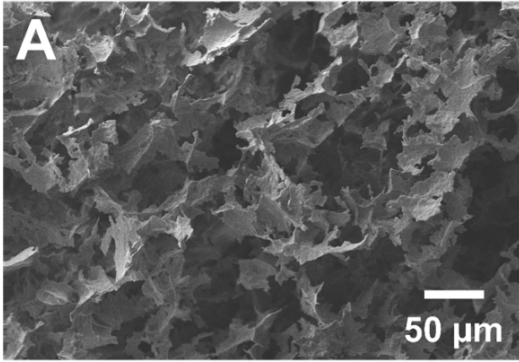
725

726

727

728

729

730

731

732

733

734

735

736

737 **Figure 4**

738

A

B

C

2 µm

0.2 µm

0.2 µm

739
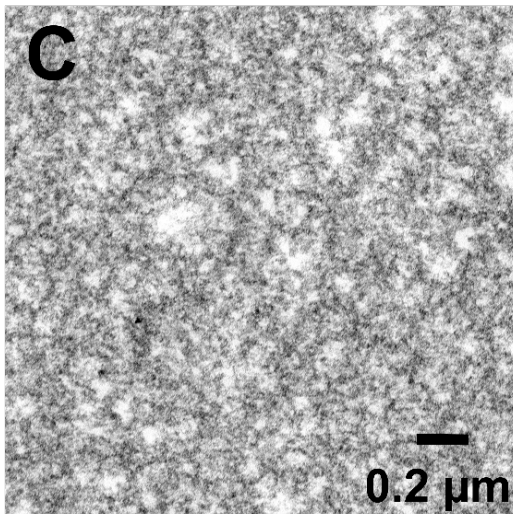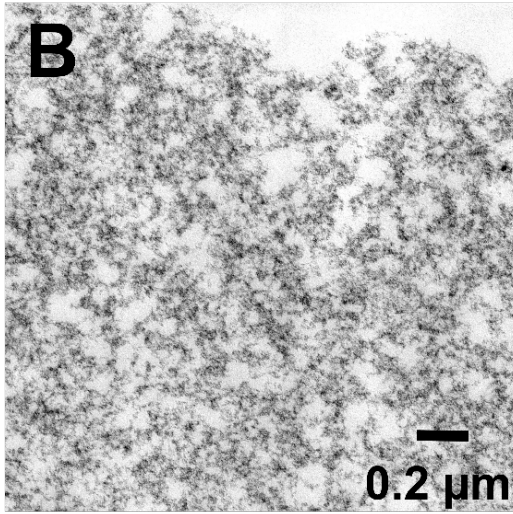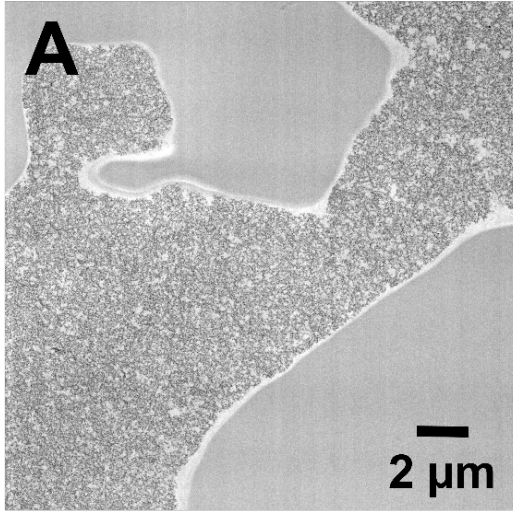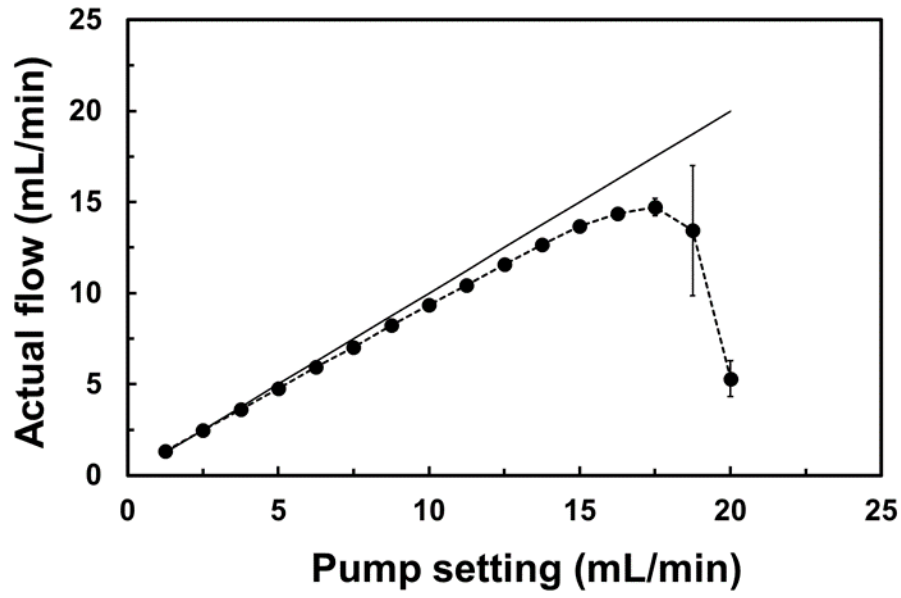
Figure 5

741

742

743

744

745

746

747

748

749

750

751

752

753

754

755 **Figure 6**

756
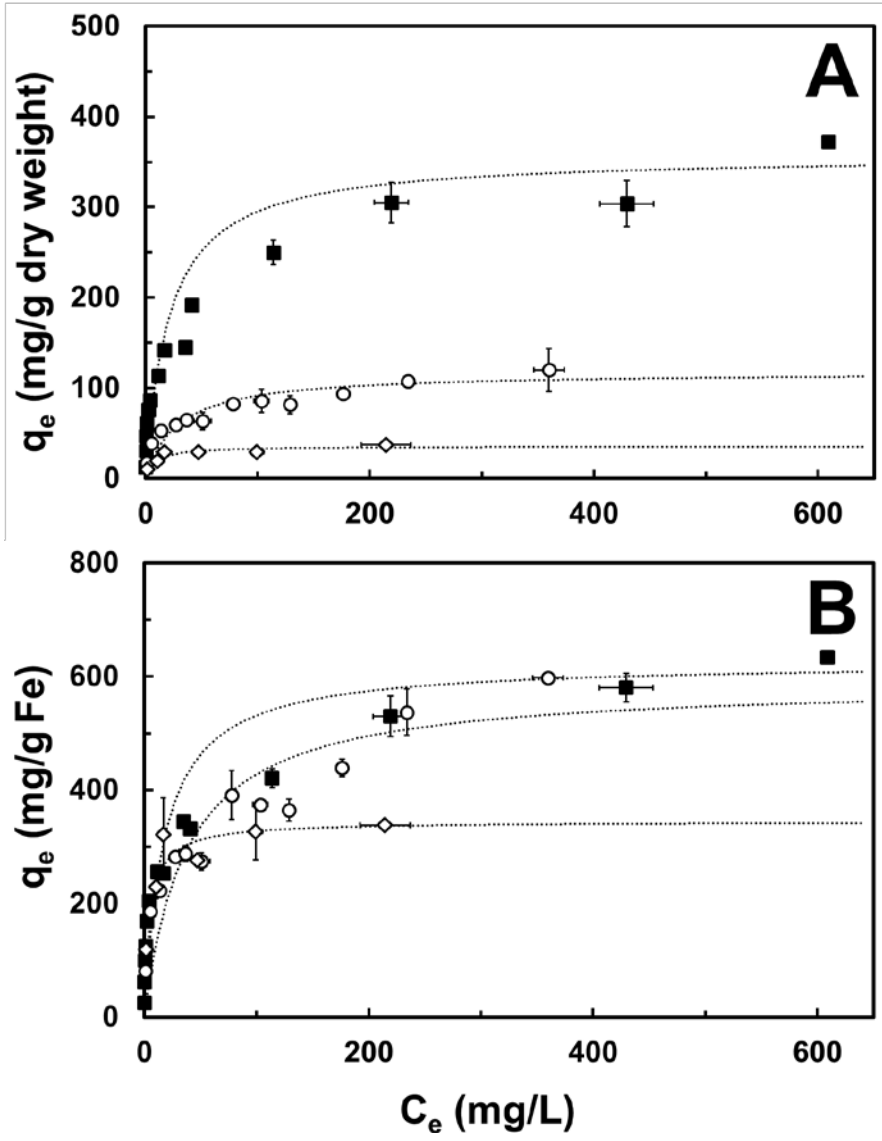
757

758

759

760

761

762

763

764   **Figure 7**

765
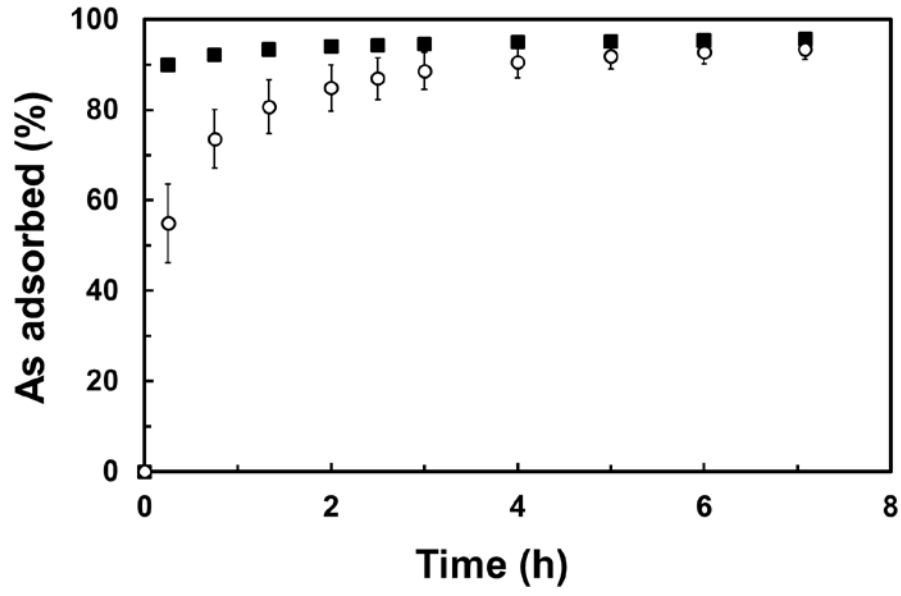
766

767

768

769

770

771

772
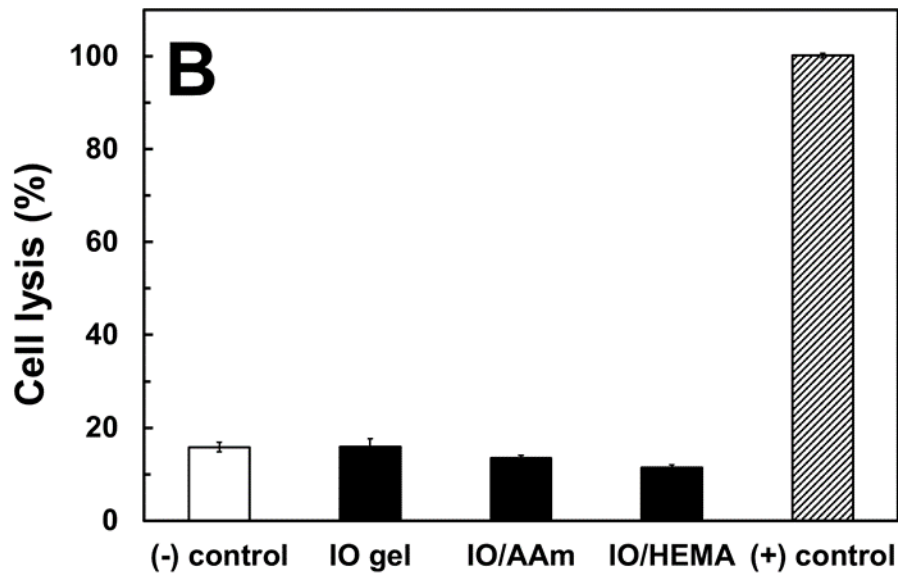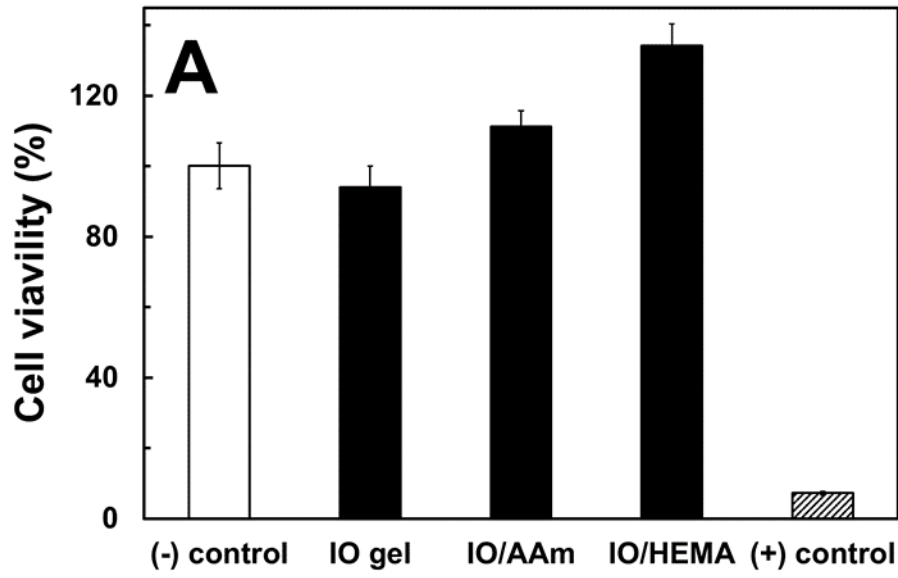
773

774

775

776

777

778

779

780   **Figure 8**

781

782

783

784

785

786

787

788   **Figure 9**

789